Supporting Information

Structure-directing role of immobilized polyoxometalates in the synthesis of porphyrinic Zr-based Metal-Organic Frameworks

Mathis Duguet, Alex Lemarchand, Youven Benseghir, Pierre Mialane, Maria-Gomez-Mingot, Catherine Roch-Marchal, Mohamed Haouas, Marc Fontecave, Caroline Mellot-Draznieks, Capucine Sassoye and Anne Dolbecq

Table of contents

Synthesis of the compounds

$((C_4H_9)_4N)_3PW_{12}O_{40}$ (named $(TBA)_3PW_{12}$)[1], tetra(4-carboxyphenyl)porphyrin (TCPP) and Fe(III) meso-tetra(4-carboxyphenyl)porphyrin (TCPP-Fe)[2] were synthesized according to reported procedures. N,N-dimethylformamide (DMF) was dried on a 4 Å molecular sieves. All other reagents were purchased from commercial sources and used without further purification.

A short heating time of 1 h was used to limit the thermodynamic phase's formation, *i.e.* **MOF-545**, in the POM@MOFs materials synthesis.

1) Synthesis of Zr_6-TCPP-25

$ZrOCl_2.8H_2O$ (50 mg, 0.155 mmol) and glacial acetic acid (4 mL) were added to DMF (7 mL) in a 25 mL scintillation vial and ultrasonically dissolved. Following sonication, the solution was incubated in a preheated oven at 130°C for 2 h. After cooling of the solution TCPP (25 mg, 0.0316 mmol) was added and the solution was stirred (~800RPM) at room temperature for 1 week in a closed vial. The microcrystalline powder was collected by centrifugation (13 000 RPM, 10 min) and washed with 11 mL of a DMF/HCl solution (prepared by mixing 1 mL of freshly prepared 1 M HCl solution and 10 mL of DMF), acetonitrile (10 mL) and acetone (10 mL). Finally, the solid was dried in an oven at 100°C overnight. This synthesis has been shown successful in conditions 6 times greater in a 100 mL round-bottom flask: $ZrOCl_2.8H_2O$ (300 mg, 0.931 mmol), glacial acetic acid (24 mL), DMF (42 mL), TCPP (150 mg, 0.190 mmol). After washing and drying a maximum amount of 196 mg of dark brown powder were recovered.

2) Synthesis of Zr_6-TCPP-Fe-25

$ZrOCl_2.8H_2O$ (50 mg, 0.155 mmol) and glacial acetic acid (4 mL) were added to DMF (7 mL) in a 25 mL scintillation vial and ultrasonically dissolved. Following sonication, the solution was incubated in a preheated oven at 130°C for 2 h. After cooling, TCPP-Fe (25 mg, 0.0284 mmol) was added and the solution was stirred (~800RPM) at room temperature for 1 week in a closed vial. The microcrystalline powder was collected by centrifugation (13 000 RPM, 10 min) and washed with 11 mL of a DMF/HCl solution (prepared by mixing 1 mL of freshly prepared 1 M HCl solution and 10 mL of DMF), acetonitrile (10 mL) and acetone (10 mL). Finally, the solid was dried in an oven at 100°C overnight. This synthesis has been shown successful in conditions 6 times greater in a 100 mL round-bottom flask: $ZrOCl_2.8H_2O$ (300

mg, 0.931 mmol), glacial acetic acid (24 mL), DMF (42 mL), TCPP-Fe (150 mg, 0.170 mmol). After washing and drying a maximum amount of 207 mg of dark brown powder were recovered.

3) Synthesis of PW_{12}@ Zr_6-TCPP-120

$ZrOCl_2.8H_2O$ (50 mg, 0.155 mmol) and glacial acetic acid (1.5 mL) were added to DMF (10 mL) in a 25 mL scintillation vial and ultrasonically dissolved. Following sonication, the solution was incubated in a preheated oven at 130°C for 2 h. After cooling, TCPP (25 mg, 0.0316 mmol) and TBA_3PW_{12} (50 mg, 0.0139 mmol) were added and the solution was further heated at 120°C for 1 h in a preheated oven. After cooling of the solution the microcrystalline powder was collected by centrifugation (13 000 RPM, 10 min) and washed with 11 mL of a DMF/HCl solution (prepared by mixing 1 mL of freshly prepared 1 M HCl solution and 10 mL of DMF), DMF (10 mL), acetonitrile (10 mL) and acetone (10 mL). Finally, the solid was dried in an oven at 100°C overnight. This synthesis has been shown successful in conditions 2 times greater: $ZrOCl_2.8H_2O$ (100 mg, 0.310 mmol), glacial acetic acid (3 mL), DMF (20 mL), TCPP (50 mg, 0.0632 mmol). After washing and drying a maximum amount of 49 mg of dark brown powder were recovered.

4) Synthesis of PW_{12}@ Zr_6-TCPP-Fe-120

$ZrOCl_2.8H_2O$ (50 mg, 0.155 mmol) and glacial acetic acid (1.5 mL) were added to DMF (10 mL) in a 25 mL scintillation vial and ultrasonically dissolved. Following sonication, the solution was incubated in a preheated oven at 130°C for 2h. After cooling, TCPP-Fe (25 mg, 0.0284 mmol) and TBA_3PW_{12} (25 mg, 0.0069 mmol) were added and the solution was further heated at 120°C for 1 h in a preheated oven. After cooling of the solution the microcrystalline powder was collected by centrifugation (13 000 RPM, 10 min) and washed with 11 mL of a DMF/HCl solution (prepared by mixing 1 mL of freshly prepared 1 M HCl solution and 10 mL of DMF), DMF (10 mL), acetonitrile (10 mL) and acetone (10 mL). Finally, the solid was dried in an oven at 100°C overnight. This synthesis was successful in conditions 2 times greater: $ZrOCl_2.8H_2O$ (100 mg, 0.310 mmol), glacial acetic acid (3 mL), DMF (20 mL), TCPP-Fe (50 mg, 0.0568 mmol). After washing and drying a maximum amount of 71 mg of dark brown powder were recovered.

The stepwise analysis presented in Figure 3 of the main text was conducted as follows:

$ZrOCl_2.8H_2O$ (50 mg, 0.155 mmol) and glacial acetic acid (1.5 mL) were added to DMF (10 mL) in 6 identical 25 mL scintillation vials and ultrasonically dissolved. Following sonication, the solutions were incubated in a preheated oven at 100°C for 1 h. After cooling, TCPP-Fe (25 mg, 0.0284 mmol) and TBA_3PW_{12} (0, 3, 8, 18, 30 and 50 mg) were added and the solutions were further heated at 120°C for 1 h in a preheated oven. After cooling of the solutions the microcrystalline powders were collected by centrifugation (13 000 RPM, 10 min) and washed with 15 mL of a DMF/HCl solution (prepared by mixing 1 mL of freshly prepared 1 M HCl solution and 10 mL of DMF), DMF (10 mL), acetonitrile (10 mL) and acetone (10 mL). Finally, the solids were dried in an oven at 100°C overnight.

Materials and Methods

Infrared (IR) spectra were recorded on a Nicolet 30 ATR 6700 FT spectrometer. Powder X-ray diffraction (PXRD) data were obtained on a Bruker D5000 diffractometer using Cu radiation (1.54059 Å). Energy dispersive spectroscopy (EDS) measurements were performed on a JEOL JSM 5800LV apparatus. C, H, N analyses were performed by Service Chromato-Masse Microanalyse (UMR 8076), Faculté de Pharmacie, 92290 Chatenay-Malabry, France. N_2 adsorption isotherms were obtained at 77 K using a TriStar II from Micromeritics after activitation with a Smart VacPrep from Micromeritics. Before the analysis, approximately 50 mg of samples were heated at 120 °C under primary vacuum over 5h.

Cyclic Voltammetry (CV)

All CV experiments were performed on SP 300 Biologic potentiostat (Bio-Logic Science Instruments SAS) in a conventional three-electrode single-compartment cell at room temperature. A flame annealed platinum wire was used as a counter electrode, a saturated Ag/AgCl/KCl electrode separated by a salt bridge as reference electrode. Glassy carbon electrode (GCE) of 3 mm diameter was used as working electrodes and was polished on wet polishing cloth using a 1 μm diamond suspension (Struers), sonicated for 30 seconds, thoroughly rinsed with ethanol and dried prior experiments. Thin films of **PW_{12}@Zr_6-TCPP-Fe-120** and **PW_{12}@Zr_6-TCPP-120** were prepared by dispersion of 1 mg of product in 200 μL of dichloroethane by sonication for 20 min and drop casting 10 μL of this suspension on the glassy carbon electrode (final mass 50 μg). The drop was allowed to dry at room temperature. Solutions of acetonitrile containing 0.1 M tetrabutylammonium perchlorate [TBA][ClO_4] or tetrabutylammonium hexafluorophosphate [TBA][PF_6] as supporting electrolyte were freshly prepared and degassed with a N_2 flux for 20 min prior each experiment. Anhydrous acetonitrile of 99.99 % purity (ACN) and supporting electrolytes were purchased from Sigma-Aldrich. Scan rate for recording the CVs was 0.1 Vs^{-1}, third scan is shown.

Solid-State NMR experiments

^1H and ^{31}P MAS NMR spectra were recorded on a Bruker AVANCE-500 spectrometer (Larmor frequencies of 500.163 MHz and 202.465 MHz, respectively) at 292 K using a 2.5 mm MAS probe. The following conditions were used for recording the ^1H MAS NMR spectra: the length of 90° ^1H pulse was 2.1 μs, and the delay time between scans was 7 s, which satisfied the 5 x T_1 condition. Sixty-four scans were collected for each 1D ^1H MAS

NMR spectra. ^{31}P MAS NMR spectra with high-power proton decoupling were recorded with cross-polarization (CP). The following conditions were used for recording the spectra with CP both in 1D and in 2D ^{1}H–^{31}P heteronuclear correlation (HETCOR) NMR experiments: the proton radiofrequency (rf) field was 75 kHz, and the contact time was 10 ms at the Hartmann−Hahn matching condition of 64 kHz. In these experiments a high-power proton decoupling of 50 kHz rf field was used only during the acquisition time. Eighty scans were collected for each 1D ^{31}P CPMAS NMR spectrum. For 2D CPMAS ^{1}H–^{31}P HETCOR NMR experiments a total of 128 t_1 increments with 3200 scans each were collected. The spinning rate was 10 kHz for ^{31}P experiments, while for 1D ^{1}H MAS NMR experiments a 30 kHz spin rate was employed. ^{1}H chemical shifts were referenced with respect to TMS, whereas ^{31}P chemical shifts to 85% H_3PO_4, as external standards, respectively, with an accuracy of ±0.5 ppm.

DFT Calculations

Structure optimization of MOF-525. MOF-525's crystal structure was originally solved by Morris *et al.*[3] by combining the construction of an initial model reflecting the connectivity of the MOF's building blocks - i.e. the $Zr_6O_4(OH)_4$ inorganic brick and the porphyrin organic linkers - and its Rietveld refinement against the experimental X-ray diffraction powder pattern. A good agreement was obtained between the simulated X-ray powder pattern and the experimental data thus validating the average MOF-525 structure (cubic system, *P*m3m, n°221) with an optimized cell parameter of 19.393 Å. For the PDF analysis, we used the reported crystal structure of MOF-525 to perform its DFT-level optimization then simulate the related PDF profile. Notably, considering the local structure of the reported $Zr_6O_4(OH)_4$ oxocluster in MOF-525, the model proposed by Morris *et al.* presents a single crystallographic position for describing the eight O atoms contained in the inner $Zr_6O_4(OH)_4$ cluster, resulting in 8 identical Zr-O distances and a high symmetry of the reported MOF-525 crystal structure (Fig. S6a). Prior DFT calculations, missing hydrogens were considered to ensure the charge balance whereby hydroxyl groups were created on half of the oxygen atoms of the Zr_6-oxocluster, resulting in 4 hydroxyl μ_3-OH groups per unit cell.

The obtained modified structure was optimized at the dispersion-corrected DFT-D3 level calculations with the Vienna *Ab initio* Simulation Package VASP.[4,5] A planewave basis set with the projector augmented wave (PAW) scalar-relativistic pseudopotentials[6] was employed for all geometry and electronic calculations. The electron-ion interactions were described by the PAW method in the implementation of Kresse and Joubert.[7] Geometry optimizations were

performed with the Perdew-Burke-Ernzerhof (PBE) exchange-correlation functional.[8] The long-range weak dispersion interactions were taken into account using the semi-empirical VdW method of Grimme DFT-D3.[9] A plane-wave cutoff of 400 eV, for the construction of the electronic wave functions, was suitable for convergence of the system. The integration over the irreducible Brillouin zone was carried out using the gamma point. Atomic positions were optimized until the forces on all atoms were smaller than 0.02 eV $Å^{-1}$.

In the DFT-optimized MOF-525, at least two types of O (Zr-(μ_3-O) and Zr-(μ_3-OH)) have to be considered leading to two types of Zr-O distances in the clusters.[10] These rather small changes in the Zr-O interatomic distances induce a local structural rearrangement of the Zr-oxocluster (Figure S6b) and a reduction of the symmetry from the symmetry group O_h to D_{2d}.

Figure S7 compares in the [1-8 Å] range the PDF profiles of MOF-525 reported by Morris *et al.*,[3] (black) of the DFT-optimized MOF-525 (red) and of UiO-67's crystal structure[11] (blue), another well-known Zr-based MOF built from the same $Zr_6O_4(OH)_4$ cluster than MOF-525. UiO-67 is used here as a reference, knowing that its PDF signal will provide a univoqual signature of the $Zr_6O_4(OH)_4$ oxocluster. Interestingly, significant differences are observable whereby the global shape of the PDF of the reported MOF-525 does not match that of the UiO-67. Indeed, the peak positions of the main Zr-O and Zr-Zr distances in the reported MOF-525 are shifted to smaller values than in UiO-67, at 2.1 Å, 3.3 Å and 4.5 Å. They are also different from the values expected for this family of clusters, *i.e.* 2.2 Å, 3.5 Å and 4.8 Å.[12] The DFT-optimized MOF-525 structure underwent noticeable changes when compared to that of the reported MOF-525 (Fig. S6b). We observe a modification of the Zr-O first distances distribution and a global increase of the Zr-Zr distances leading to a comparable structure of the UiO-67's inorganic cluster (Fig. S6c). The simulated PDF of the MOF-525 obtained from DFT is plotted in Fig. S7-red. The global shape of the PDF and the peak position corresponding to the Zr-O and Zr-Zr distances are in good agreement with the features observed for UiO-67 (Fig. S7-blue) and found in the literature[11–14]. The DFT optimization thus led to a satisfying MOF-525 structural model usable for phase identification. A similar procedure was conducted to obtain an optimized structural model for the PCN-224 crystal structure obtained from single crystal diffraction data. [15] We would like to note that the slight differences generated in the local atomic structure did not induce noticeable change on the X-ray diffraction pattern of both compounds, and so in their average structure (Fig. S8).

Docking of the PW_{12} guest into MOF-525(Fe)'s porous structure. The Chlorines coordinated to the Fe porphyrins were positioned randomly inside and outside the cubic unit cell. In view of the Infrared Spectra of the composite materials (Figure S1), the TBA molecules around the POM were considered absent after the synthesis. The POM's charge was compensated in the calculation by the addition of 3 protons. To determine the preferential places of those hydrogens 4 different configurations of hydrogens on bridging oxygens of the POM were tested. The POM was placed in a bounding box big enough to prevent interactions and was optimized on VASP with the GGA-PBE DFT functional with a planewave cut-off of 400eV. The most stable structure was used in the following calculations. In a first step, the position and orientation of the guest POM were sampled during a simulated annealing procedure, allowing visiting the void volume of MOF-525(Fe) (*i.e.* the cubic cages). Non-bonded interaction energies between the POM and the hybrid MOF-525(Fe) framework were described with the *cvff* forcefield,[16] in which Van der Waals (Lennard-Jones potentials) and electrostatic interactions were explicitly included. The atomic charges for the POM and the MOF-525(Fe) were calculated by the charge-equilibration method. In a second step, low energy PW_{12}@MOF-525(Fe) candidates were extracted from the SA results and further optimized with the same method as MOF-525(Fe). Once the optimization completed, the interaction energy (or binding energy) between the POM and the MOF-525(Fe) host was then estimated through single-point calculations, yielding an interaction energy around -422 $kJ.mol^{-1}$. For comparison, the same calculations on the Fe-free MOF-525 provided a much lower interaction energy, estimated around -64 $kJ.mol^{-1}$.

Pair Distribution Function Analysis

Data collection and sample preparation. X-ray total scattering data were measured with a Bruker D8 ADVANCE diffractometer equipped with a focusing Göbel mirror and a LYNXEYE detector, with Mo Kα radiation (mean λ(Kα1α2) = 0.71073 Å) at room temperature. The sample preparation consists first in a supercritical CO_2 washing/activation step of the samples to remove all the solvent molecules inside the MOF pores after the synthesis. Then, inside a glovebox under Ar atmosphere, a few tens of milligrams of powder are placed in a thin-walled (0.01 mm) borosilicate glass capillary of 1.0 mm diameter. Measurements were performed from Q_{min} = 0.12 $Å^{-1}$ to Q_{max} = 17.0 $Å^{-1}$ ($Q = 4\pi \sin\theta/\lambda$) with sample rotation around its axis and evolving counting parameters in function of Q-range to optimize the counting rate at high Q. The final XRD diagram was thus obtained from the combination of 7 patterns, converted in counts per second, with the following parameters

2θi(°)-2θf(°)-step size(°)-step time(s): 0.8-31-0.02-2, 29-61-0.04-6, 59-91-0.06-15, 89 121 0.1 40 (twice) and 119-150-0.1 100 (twice) for a total measuring time of 34 hours. Additional scattering measurements from empty capillary were performed in the same conditions for background subtraction. Raw data were treated using the PDFgetX3 program.[17] Standard corrections were applied to the total scattering data. After a normalization step, they were reduced into the structure function. The total PDF G(r) is finally obtained by a Fourier Transform (FT).

d-PDF calculation and refinement. The experimental differential PDFs (d-PDFs) were obtained by subtraction of the **Zr_6-TCPP-Fe-25**'s PDF from that of the **PW_{12}@ Zr_6-TCPP-Fe-120**. The d-PDF was refined with a $PW_{12}O_{40}^{3-}$ structural model using the DIFFEV software included in the DISCUS suite package.[18,19] The initial $PW_{12}O_{40}^{3-}$ structural model was built from the crystalline structure of $H_3PW_{12}O_{40}$. $6H_2O$ with the space group Pn-3m (n°224) (cubic) (JCPDS 00-050-0304)[20] removing the structure water molecules and the 3 protons which compensate the POM negative charge, using the DISCUS software. The refinement was performed according to the procedure described by Neder and Proffen. [18,19] The following parameters were refined considering the POM symmetry: the scale factor, the atomic positions (other than particular positions), the isotropic atomic displacement parameters (Biso) and the dynamic correlation factor (δ2). The interval in which the atomic position of the terminal oxygen O_t can vary has been constrained to maintain a distance W-O_t consistent with a double bond W=O (around 1.7 Å). Metallic silicon (Si) served as a standard material to determine the experimental resolution effect factor Q_{damp} (refined Q_{damp} = 0.028 $Å^{-1}$).

PDF calculations from structural models. The simulated PDF profiles of MOF-525 and PCN-224 DFT models were performed using the PDFgui software with periodic boundary conditions[21]. For each atom types, small isotropic atomic displacements ($U=U_{11}=U_{22}=U_{33}$ with U_{Zr} = 0.003 Å², $U_O = U_C = U_N = U_H$ = 0.006 Å²) were considered in the calculation to obtain a PDF peak broadening consistent with experiment. The $[PW_{12}O_{40}]^{3-}$ reference model was obtained from the CIF file of $H_3PW_{12}O_{40}$, $6H_2O$ crystalline structure (JCPDS 00-050-0304) [20]. The PDF calculations were performed using PDFgui[21] with a damping coefficient corresponding to a particle size of 12 Å. For each atom types, small isotropic atomic displacements ($U=U_{11}=U_{22}=U_{33}$ with U_W=0.001 Å², U_O=0.010 Å², U_P=0.006 Å²) were considered in the calculation to obtain a PDF peak broadening consistent with experiment.

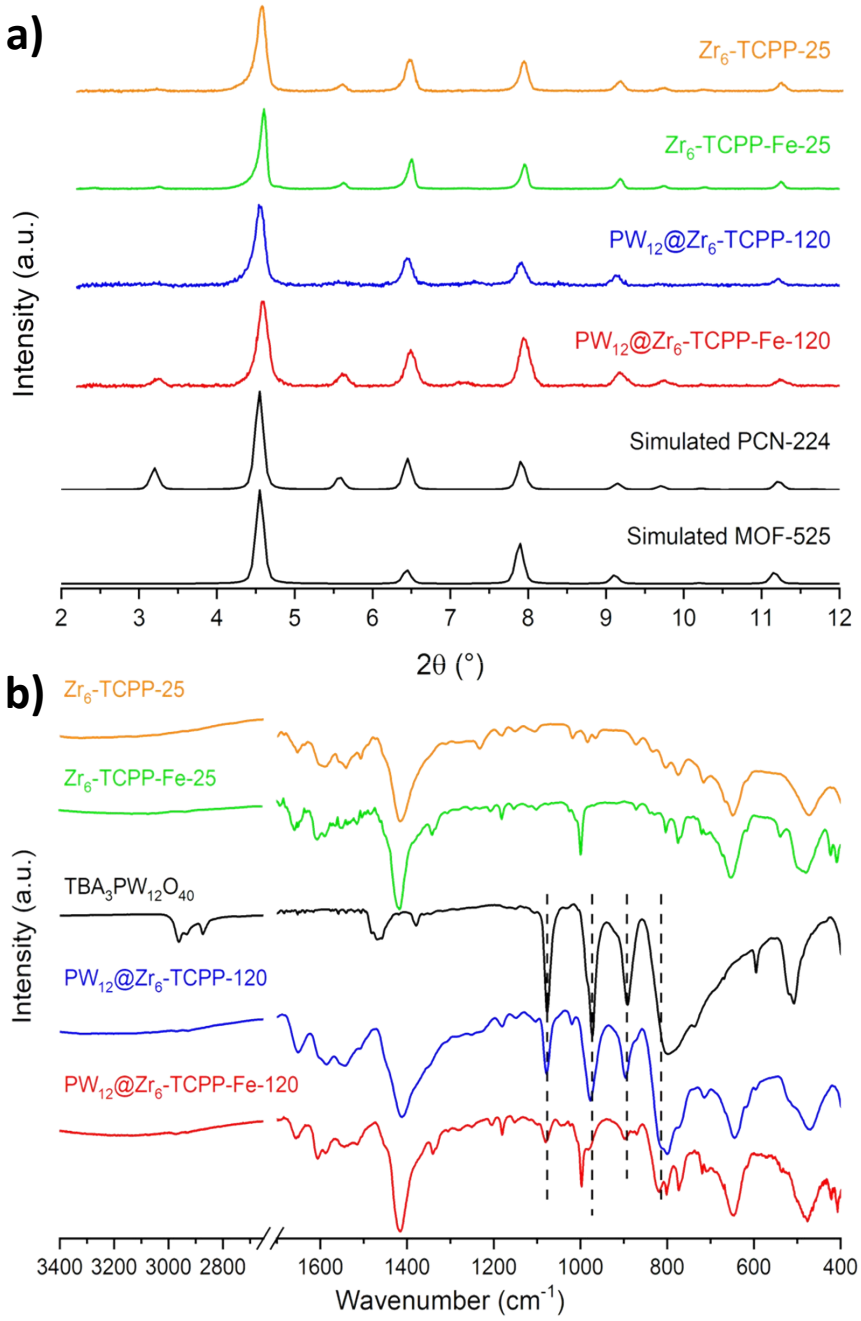

Figure S1. General XRD diagrams and IR spectra. (a) Powder X-ray diffraction diagrams of the four compounds synthesized in this study, *i.e.* the two POM-free **Zr_6-TCPP-25**, **Zr_6-TCPP-Fe-25** synthesized at room temperature, and their **PW_{12}@Zr_6-TCPP-120** and **PW_{12}@Zr_6-TCPP-Fe-120** counterparts synthesized at high temperature (using 50 and 25 mg of POM respectively). In black the simulated powder diagrams of the free-base **MOF-525** and **PCN-224**; (b) IR spectra of the five compounds. The characteristic bands of the POM are indicated with black dashed lines.

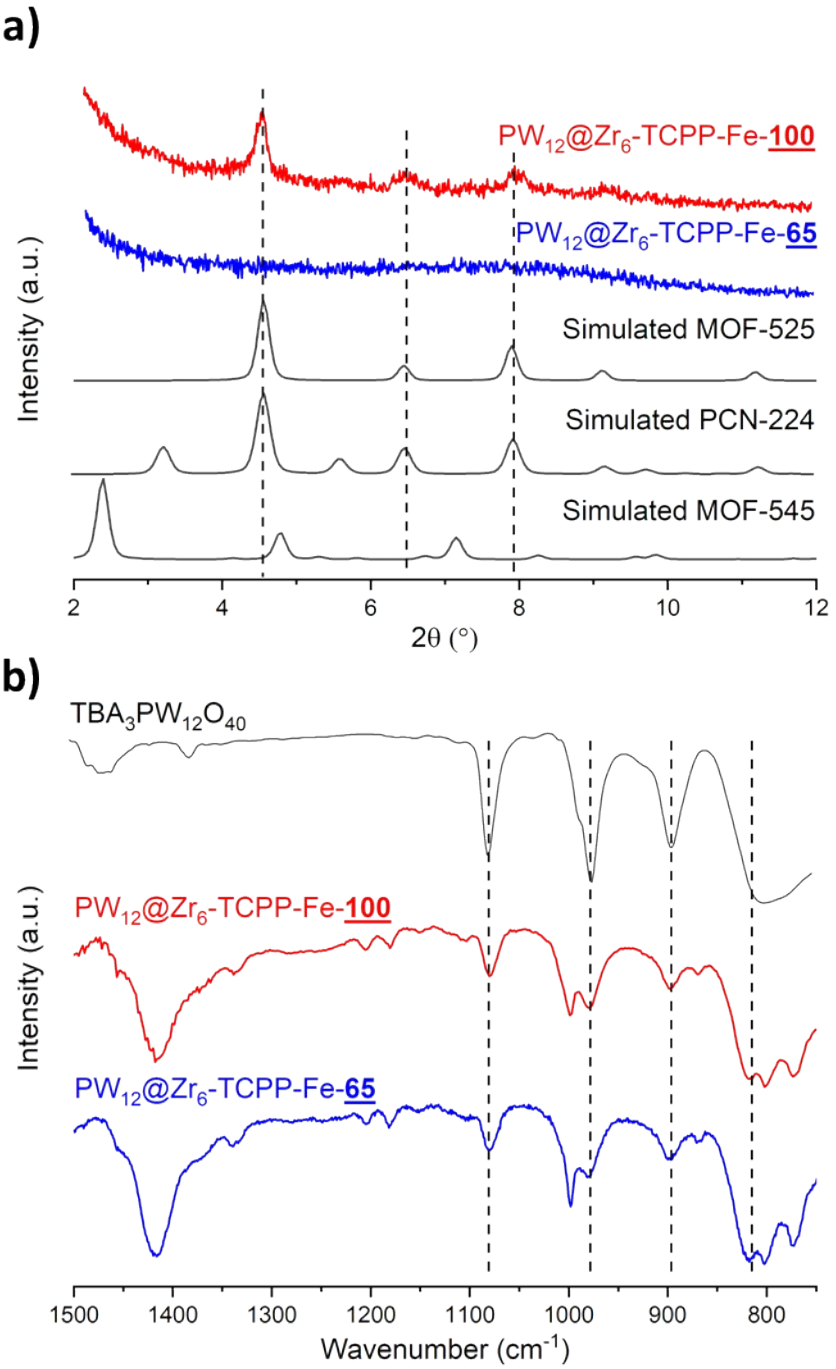

Figure S2. Analysis of composite materials **PW_{12}@Zr_6-TCPP-Fe-T** (with T = 100, 65°C) (a) XRD diagrams and (b) IR spectra.

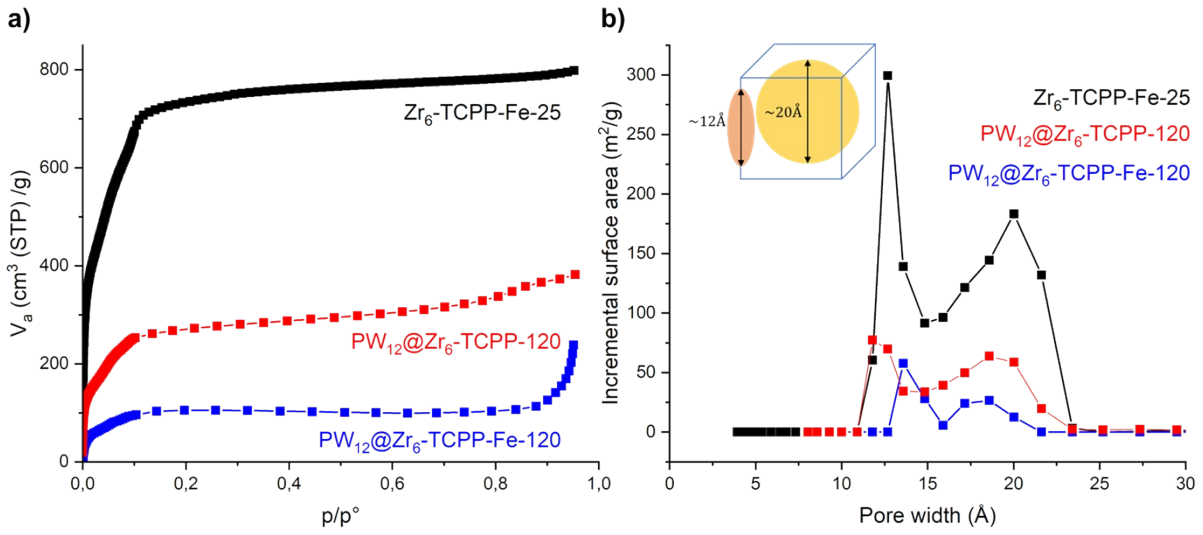

Figure S3. BET and pore distribution of POM@MOF composites. (a) N_2 adsorption isotherms of **Zr_6-TCPP-Fe-25**, **PW_{12}@Zr_6-TCPP-120** and **PW_{12}@Zr_6-TCPP-Fe-120** composites (77 K, P/P_0 = 1 atm). (b) Pore size distribution in the three systems.

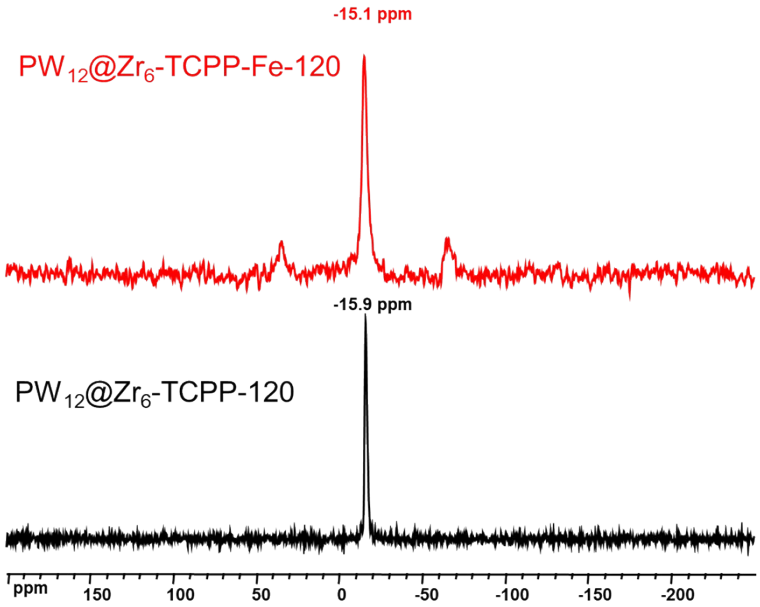

Figure S4. Solid-State $^{31}P\{^1H\}$ NMR CPMAS 10 kHz spectra of **PW_{12}@Zr_6-TCPP-120** and **PW_{12}@Zr_6-TCPP-Fe-120**. The unique ^{31}P signal is a typical signature of the $[PW_{12}O_{40}]^{3-}$ POM.[1] Note that the line broadening and the spinning sideband observed in the spectrum of **PW_{12}@Zr_6-TCPP-Fe-120** are due to the increase of chemical shift anisotropy occurring from interactions of ^{31}P nuclei of the POM with paramagnetic species Fe^{III}.

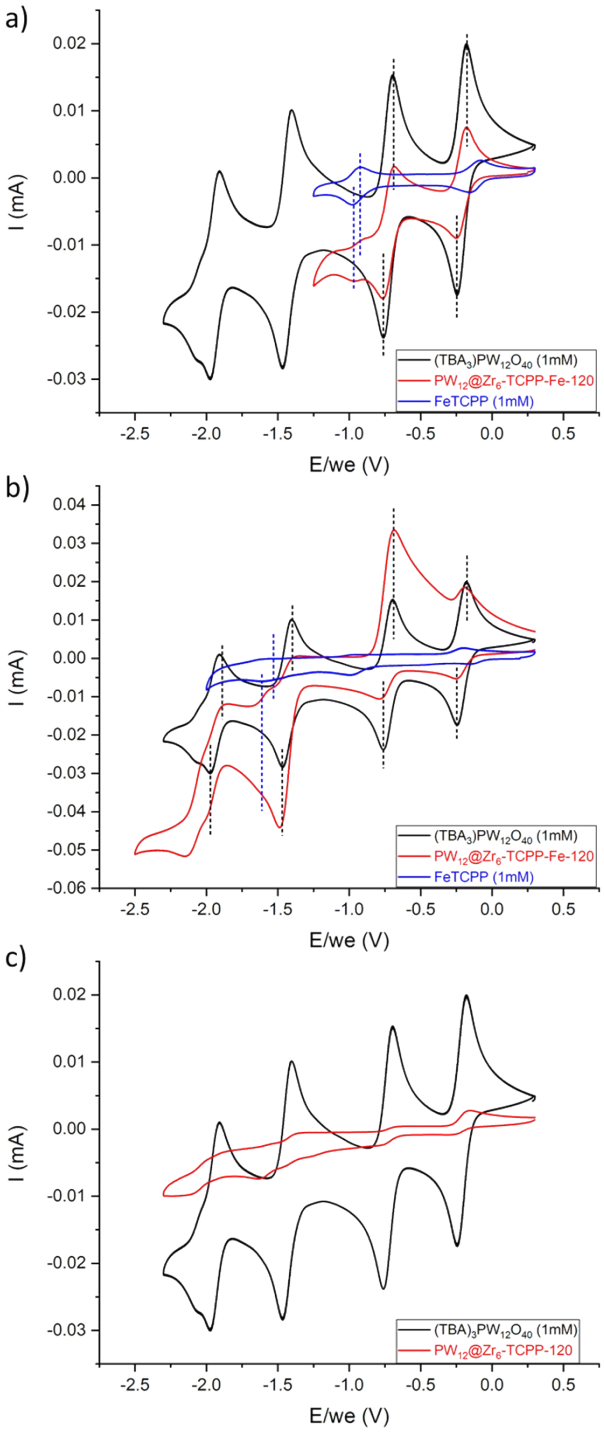

Figure S5. Cyclic voltammograms in acetonitrile of 1 mM $PW_{12}O_{40}^{3-}$ in solution (black), thin film of **PW_{12}@Zr_6-TCPP-Fe-120** (red) and 1 mM TCPP-Fe in solution (blue) at short range of potentials (a) and long range of potentials (b). c) CVs of 1 mM $PW_{12}O_{40}^{3-}$ in solution (black) and thin film of **PW_{12}@Zr_6-TCPP-120** (red). The supporting electrolyte used was 0.1 M [TBA][ClO_4] for the CVs of $PW_{12}O_{40}^{3-}$ in solution and 0.1 M [TBA][PF_6] for the rest of experiments. Dark dashed lines highlight the similarities between the POM and the **PW_{12}@Zr_6-TCPP-Fe-120** composite, the reduction potentials are listed in Table S3. Blue dashed lines highlight the similarities between the TCPP-Fe and the **PW_{12}@Zr_6-TCPP-Fe-120** composite.

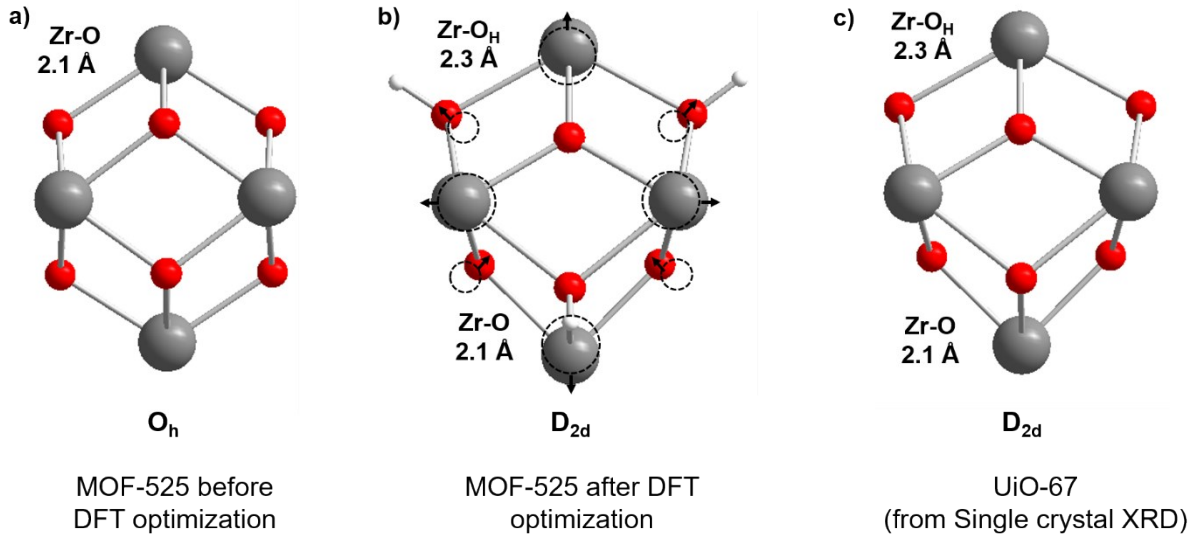

Figure S6. Structure of Zr_6-oxoclusters for the crystal structure of (a) MOF-525 reported by Morris *et al.*[3] before the DFT geometry optimization, (b) MOF-525 after DFT geometry optimization and (c) UiO-67 obtained from CIF structure file (Single crystal X-ray diffraction).[11] Zirconium, oxygen and hydrogen are respectively grey, red and white. Hydrogen atoms were only considered in the case of the structural model obtained from DFT geometry optimization because Hydrogen is not visible through X-ray diffraction technics. Black dotted circles and black arrows illustrate the initial atom position before the DFT geometry optimization and their displacements upon the DFT geometry optimization.

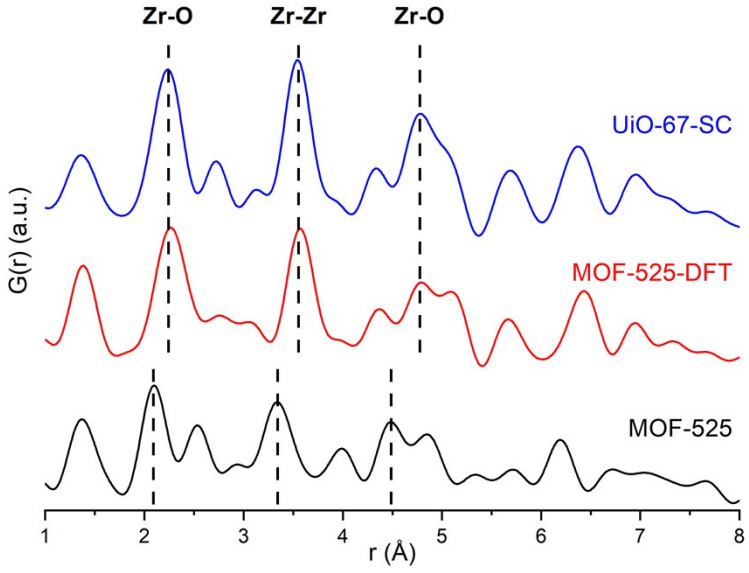

Figure S7. Simulated PDF profiles from the structural model of (black) MOF-525 reported from Morris *et al.*[3], (red) MOF-525 after DFT optimization and (blue) UiO-67 obtained from CIF structure file (single crystal (SC) X-ray diffraction).[11] Black dotted lines correspond to various Zr-O and Zr-Zr distances respectively at 2.2, 3.5 and 4.8 Å for UiO-67-SC and MOF-525-DFT and at 2.1, 3.3 and 4.3 Å for MOF-525.

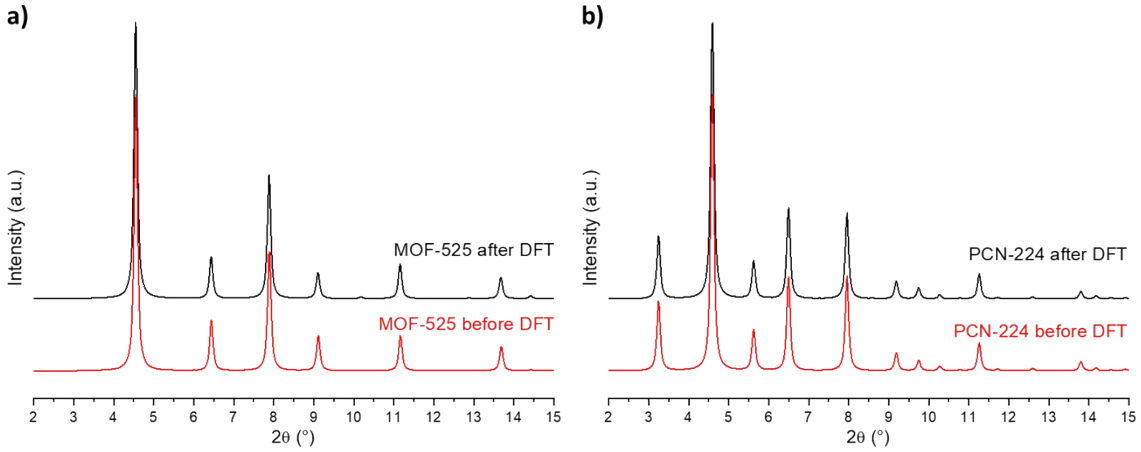

Figure S8. Simulated XRD patterns from (a) MOF-525 and (b) PCN-224 before (red) and after (black) DFT geometry optimization. The XRD patterns were simulated using Mercury software with Cu Kα (1.54056 Å).[22]

Comments on the simulated PDF profiles of MOF-525 and PCN-224 obtained from DFT geometry optimizations

The DFT-optimization step was crucial in obtaining a correct structural model of MOF-525 reflecting the difference between the Zr-O and Zr-OH distances within the $Zr_6O_4(OH)_4$ oxocluster and their impact on the whole crystal structure (see the *Structure optimization of MOF-525* part for details). The simulated PDFs of MOF-525 and PCN-224 both optimized by DFT are plotted in Fig. S9 in the [1-8 Å] range. As expected from their common Zr-oxocluster, the PDF of MOF-525 and PCN-224 crystal structures exhibit common intense peaks at 2.2 Å, 3.5 Å and 4.8 Å which emanate from the various characteristic Zr-O and Zr-Zr distances within the $Zr_6O_4(OH)_4$ units (black dashed lines, Fig. S9). A series of less intense peaks in PCN-224 when compared to MOF-525 positioned at 3.1, 4.4, 5.1 and 6.3 Å correspond to characteristic Zr-C distances between the Zr atoms and the lighter ones (C, N, H) of the TCPP-linker (red dashed lines, Fig. S9). Although they are observable in both PDFs, these peaks are notably more intense in MOF-525 than in PCN-224. This significant intensity difference emanates from the lack of 50% TCPP linkers in PCN-224 with respect to MOF-525. Illustratively, the PDF peak at 5.1 Å is rather intense and distinct in MOF-525, while identified in PCN-224 as a shoulder of the neighbouring peak at 4.8 Å. These missing linkers imply the presence of hydroxyl groups or water molecules on the inner cluster Zr-atoms to ensure the charge balance in PCN-224. This may explain the slight increase in intensity of the PDF peak positioned at 4.0 Å assigned to the Zr-O distances in PCN-224 with respect to that observed in MOF-525. Based on these features, we are able to distinguish one phase from the other in a sample from the fine analysis of its experimental PDF.

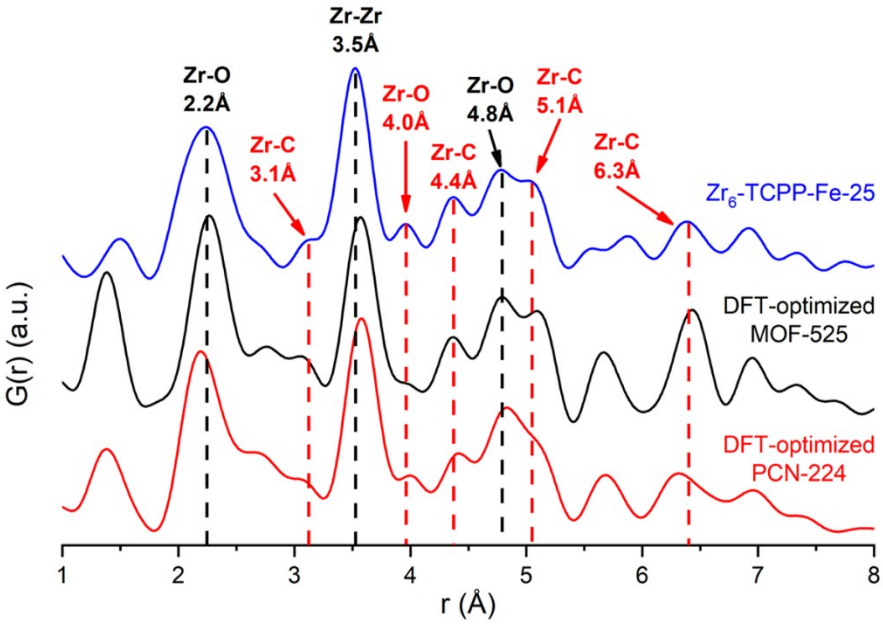

Figure S9. Experimental PDF profile of Zr_6-TCPP-MOF and simulated PDFs profiles of MOF-525 and PCN-224 obtained from DFT-level geometry optimizations. Black dashed lines correspond to Zr-O and Zr-Zr characteristic distances in the core of the $Zr_6O_4(OH)_4$ clusters. Red dashed lines correspond to Zr-C and Zr-O distances susceptible to vary from **MOF-525** to **PCN-224**.

Comments on the Experimental Differential PDF Calculation and Data Description

The experimental PDF of **Zr_6-TCPP-Fe-25** exhibits all short-range order characteristics of **Zr_6-TCPP-MOF-Fe** (Figure S10. red line). The absence of intense peaks at middle- and long-range order in the sample indicates a loss of order for higher radial distances reflecting a relatively poor crystallinity and a certain flexibility of the structure. The experimental PDF of **PW_{12}@Zr_6-TCPP-Fe-120** (Figure S10. black line) exhibits very intense and narrow additional peaks below 8.0 Å assigned to the presence of the PW_{12} moieties. It undergoes then a strong dampening. At higher radial distances, the absence of intense peaks shows the poor crystallinity of the sample. Nevertheless, the experimental PDFs of the two samples overlap perfectly at high r distances, both exhibiting the same low intensity oscillatory behavior characteristic of porous MOFs. This long-range feature allows the calculation of the experimental differential PDF. The related experimental d-PDF (Figure S11, blue curve) is thus mainly dominated by intense and narrow peaks below 8.0 Å followed by a strong dampening. Comparing the experimental d-PDF to the calculated PDF of an isolated PW_{12} from reported crystallographic data[20] (Figure S11, black curve), peak assignment was performed. The two first peaks (A, B) at 2.0 Å and 2.5 Å correspond to various W-O bond lengths of the WO_6 octahedra in the POM structure. The following intense peaks positioned at 3.4, 3.7, 5.0, 6.2 and 7.2 Å (C to G) correspond to various W-W distances inside the PW_{12} structure[23]. Unfortunately, it was impossible to observe the characteristic peak of the P-O bond length at 1.5 Å. As previously stated, it is tough to obtain reliable data on the *r*-range below 1.5 Å from laboratory X-ray total scattering instruments.

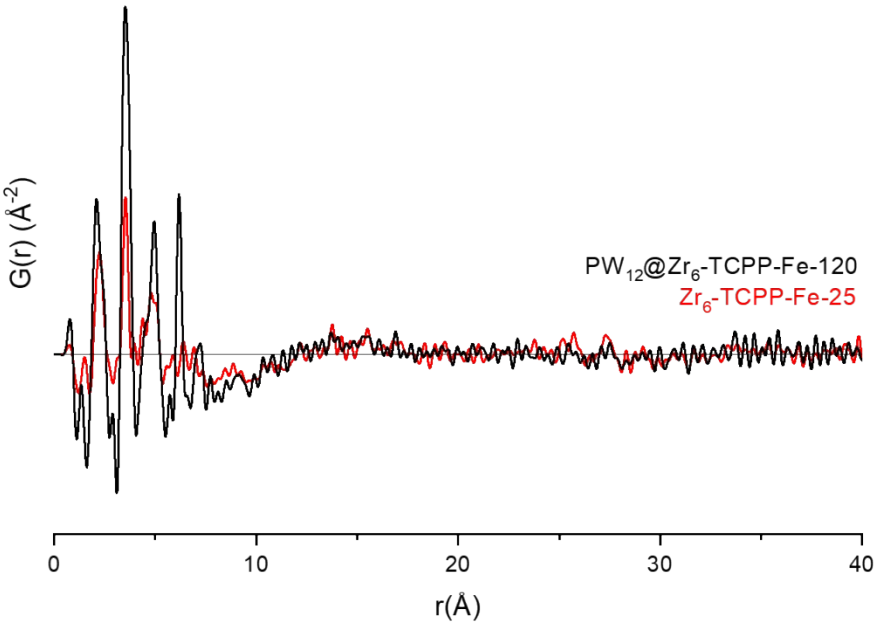

Figure S10. Experimental PDF data of **Zr_6-TCPP-Fe-25** (red line) and **PW_{12}@Zr_6-TCPP-Fe-120** (black line).

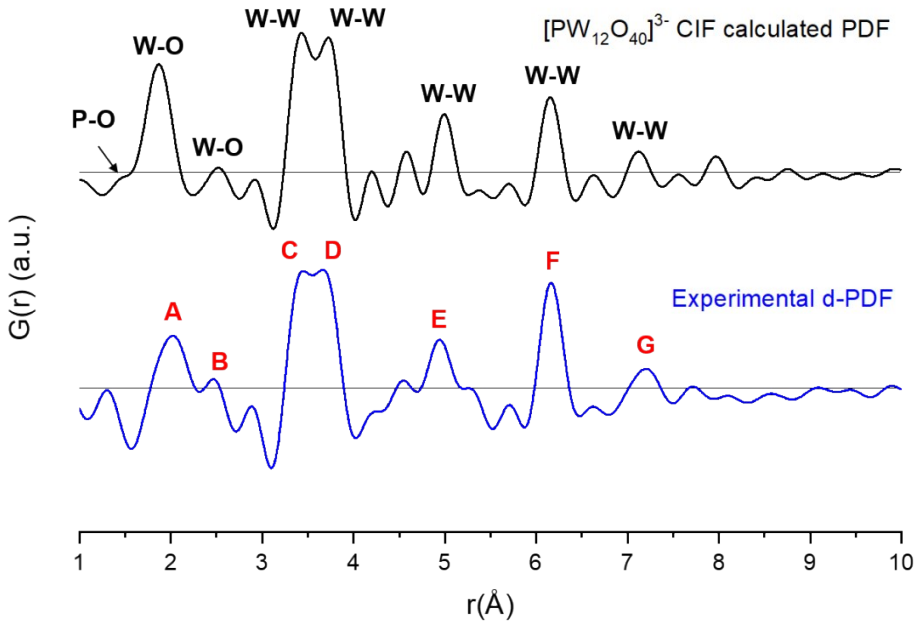

Figure S11. Comparison of the calculated PDF of an isolated PW_{12} from reported crystallographic data[20] and the experimental d-PDF associated to PW_{12} in **PW_{12}@Zr_6-TCPP-Fe-120**. A-H labels of peaks correspond to characteristic distances in the POM structure.

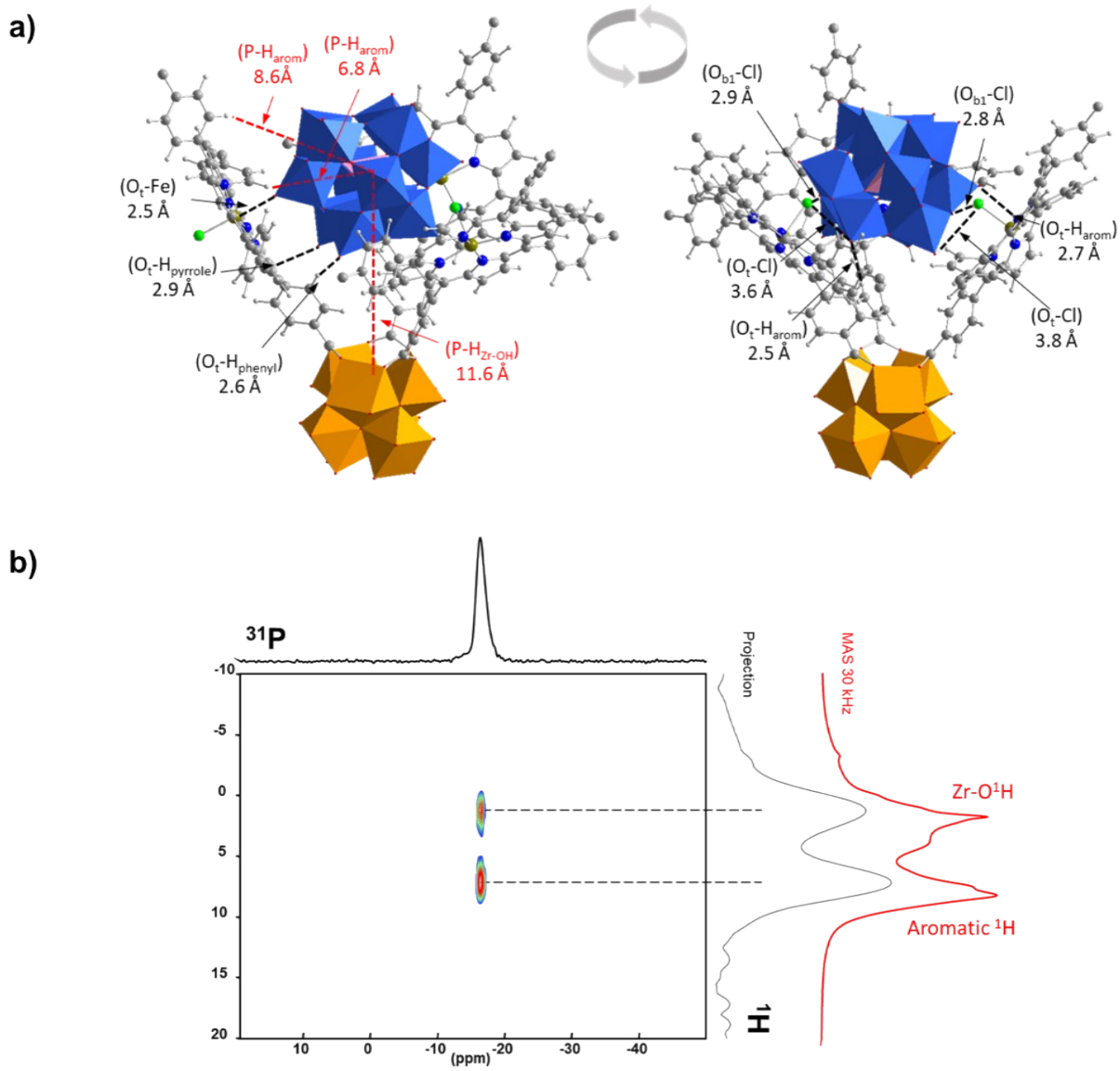

Figure S12. Interaction of the POM with the MOF host from (a) Density Functional Theory calculations performed on MOF-525-Fe (inside point of view of the interaction between the POM and the inorganic matrix) and (b) 2D $^{31}P\{^{1}H\}$ HETCOR Solid-State NMR CPMAS 10 kHz of **PW_{12}@Zr_6-TCPP-120** (the HETCOR NMR data collection could not be performed on the Fe-metallated form due to its paramagnetism).

Table S1. EDS and C, H, N analyses of POM@MOFs

As previously discussed, the TBA were considered absent of the final materials. We considered that the charge compensation of the POM in the material came from ligand defects evidenced by the following analysis. The formula of the Zr_6-TCPP MOF was taken from the literature[24]: $[Zr_6O_4(\mu_3\text{-}OH)_4(P)_x(\mu_1\text{-}OH)_{4(3-x)}(\mu_1\text{-}H_2O)_{4(3-x)}]$, where P denotes the TCPP linkers that connect the octahedral Zr_6 nodes. The value of x and of the amount of POM were deduced from a combination of C, H, N, EDS analysis and electroneutrality considerations.

PW_{12}@ Zr_6-TCPP-120:

$Zr_6O_4(OH)_4(OH)_{2.5}(H_2O)_{2.5}(C_{48}H_{26}O_8N_4)_2(PW_{12}O_{40})_{0.50}(DMF)_3(H_2O)_{26}$ (M = 4464.3 g mol^{-1})

Electroneutrality check:

6x4 – 8 – 4 - 2.5 - 2x4 - 0.50x3 = 0

	Calc	Exp
W/Zr	1.00	1.03

	Calc	Exp
C	28.23	26.35
H	3.08	2.76
N	3.45	3.96

PW_{12}@ Zr_6-TCPP-Fe-120:

$Zr_6O_4(OH)_4(OH)_{3.96}(H_2O)_{3.96}(C_{48}H_{24}O_8N_4FeCl)_{1.80}(PW_{12}O_{40})_{0.28}(H_2O)_{30}$ (M = 3746.2 g mol^{-1})

Electroneutrality check:

6x4 – 8 – 4 – 3.96 - 1.80x4 - 0.28x3 = 0

	Calc	Exp
W/Zr	0.56	0.56
Fe/Cl	1.00	1.06
Fe/Zr	0.30	0.38

	Calc	Exp
C	27.74	22.23
H	2.70	1.95
N	3.21	2.91

Table S2. Structural parameters and characteristic distances of the PW_{12} polyoxometalate obtained from the d-PDF refinement associated to the PW_{12} immobilized in Zr_6-TCPP-Fe host. For a comparison purpose, the structural parameters of the isolated Keggin $PW_{12}O_{40}^{3-}$ reference extracted from its crystal structure are reminded.

Structural data		**Refined values**	**Reference (JCPDS 00-50-0304)[20]**
Structural parameters	**a** (Å)	12.156	12.156
	P $x_P = y_P = z_P$	0.750 ; 0.750 ; 0.750	0.750 ; 0.750 ; 0.750
	O_p $x_{O1} = y_{O1} = z_{O1}$	0.819	0.820
	O_2 $x_{Ob1} = y_{Ob1}$; z_{Ob1}	0.610 ; 0.475	0.656 ; 0.507
	O_3 $x_{Ob2} = y_{Ob2}$; z_{Ob2}	0.872 ; 0.032	0.870 ; 0.026
	O_t x_{O4} ; $y_{O4} = z_{O4}$	0.730 ; 0.055	0.735 ; 0.053
	W x_W ; $y_W = z_w$	0.758 ; 0.956	0.758 ; 0.957
	B_{iso} P (Å²)	1.29	0.50
	B_{iso} O (Å²)	1.50	0.47
	B_{iso} W (Å²)	0.57	1.57
First distances	**P-O_t** (Å)	1.45	1.47
	W-$Oo_{ctahedron}$ (Å)	$1.73 < d_{W-O} < 2.47$	$1.69 < d_{W-O} < 2.45$
	W-W (Å)	3.40 ; 3.68	3.40 ; 3.68
Refinement quality (R_w)		0.293	/

Table S3. Reduction peak potentials measured in the CVs in Figure S5.

Compound	**E_{Pred} vs. Ag/AgCl (KCl sat.) / V**			
$(TBA)_3PW_{12}O_{40}$	-0.243	-0.757	-1.468	-1.974
PW_{12}@Zr_6-TCPP-Fe-120	-0.245	-0.775	-1.488	-2.144
PW_{12}@Zr_6-TCPP-120	-0.258	-0.772	-1.611	-2.111

References

1 P. Souchay, *Ions Minéraux Condensés*, Paris, Masson et cie,., 1969.

2 D. Feng, Z.-Y. Gu, J.-R. Li, H.-L. Jiang, Z. Wei and H.-C. Zhou, *Angew. Chem. Int. Ed.*, 2012, **51**, 10307–10310.

3 W. Morris, B. Volosskiy, S. Demir, F. Gándara, P. L. McGrier, H. Furukawa, D. Cascio, J. F. Stoddart and O. M. Yaghi, *Inorg. Chem.*, 2012, **51**, 6443–6445.

4 G. Kresse and J. Furthmüller, *Phys. Rev. B*, 1996, **54**, 11169.

5 G. Kresse and J. Furthmüller, *Comput. Mater. Sci.*, 1996, **6**, 15–50.

6 P. E. Blöchl, *Phys. Rev. B*, 1994, **50**, 17953.

7 G. Kresse and D. Joubert, *Phys. Rev. B*, 1999, **59**, 1758.

8 J. P. Perdew, K. Burke and M. Ernzerhof, *Phys. Rev. Lett.*, 1996, **77**, 3865.

9 S. Grimme, J. Antony, S. Ehrlich and H. Krieg, *J. Chem. Phys.*, 2010, **132**, 154104.

10 P. Piszczek, A. Radtke, A. Grodzicki, A. Wojtczak and J. Chojnacki, *Polyhedron*, 2007, **26**, 679–685.

11 S. Øien, D. Wragg, H. Reinsch, S. Svelle, S. Bordiga, C. Lamberti and K. P. Lillerud, *Cryst. Growth Des.*, 2014, **14**, 5370–5372.

12 H. Xu, S. Sommer, N. L. N. Broge, J. Gao and B. B. Iversen, *Chem. – Eur. J.*, 2019, **25**, 2051–2058.

13 T. D. Bennett, T. K. Todorova, E. F. Baxter, D. G. Reid, C. Gervais, B. Bueken, B. V. de Voorde, D. D. Vos, D. A. Keen and C. Mellot-Draznieks, *Phys. Chem. Chem. Phys.*, 2016, **18**, 2192–2201.

14 Y. Benseghir, A. Lemarchand, M. Duguet, P. Mialane, M. Gomez-Mingot, C. Roch-Marchal, T. Pino, M.-H. Ha-Thi, M. Haouas, M. Fontecave, A. Dolbecq, C. Sassoye and C. Mellot-Draznieks, *J. Am. Chem. Soc.*, 2020, **142**, 9428–9438.

15 D. Feng, W.-C. Chung, Z. Wei, Z.-Y. Gu, H.-L. Jiang, Y.-P. Chen, D. J. Darensbourg and H.-C. Zhou, *J. Am. Chem. Soc.*, 2013, **135**, 17105–17110.

16 J. R. Maple, U. Dinur and A. T. Hagler, *Proc. Natl. Acad. Sci.*, 1988, **85**, 5350–5354.

17 P. Juhás, T. Davis, C. L. Farrow and S. J. Billinge, *J. Appl. Crystallogr.*, 2013, **46**, 560–566.

18 R. B. Neder and T. Proffen, *Diffuse Scattering and Defect Structure Simulations: A cook book using the program DISCUS*, Oxford University Press, 2008, vol. 11.

19 T. Proffen and R. B. Neder, *J. Appl. Crystallogr.*, 1999, **32**, 838–839.

20 A. Kremenović, A. Spasojević-de Biré, R. Dimitrijević, P. Sciau, U. B. Mioč and P. Colomban, *Solid State Ion.*, 2000, **132**, 39–53.

21 C. L. Farrow, P. Juhas, J. W. Liu, D. Bryndin, E. S. Božin, J. Bloch, T. Proffen and S. J. L. Billinge, *J. Phys. Condens. Matter*, 2007, **19**, 335219.

22 Mercury - The Cambridge Crystallographic Data Centre (CCDC), https://www.ccdc.cam.ac.uk/Community/csd-community/freemercury/, (accessed 16 March 2020).

23 Keggin J. F. and Bragg William Lawrence, *Proc. R. Soc. Lond. Ser. Contain. Pap. Math. Phys. Character*, 1934, **144**, 75–100.

24 S. M. Shaikh, P. M. Usov, J. Zhu, M. Cai, J. Alatis and A. J. Morris, *Inorg. Chem.*, 2019, **58**, 5145–5153.